The Molecular Zeeman Effect of Imines

I. Methanimine, its Molecular g-Tensor, its Magnetic Susceptibility Anisotropies, its Molecular Electric Quadrupole Moment, its Electric Field Gradient at the Nitrogen Nucleus, and its Nitrogen Spin-Rotation Coupling

H. Krause and D. H. Sutter
Institut für Physikalische Chemie, Abt. Chemische Physik, Universität Kiel,
D-2300 Kiel, West Germany

Michael H. Palmer
Department of Chemistry, University of Edinburgh, Edinburgh, EH9 3JJ, Scotland

Z. Naturforsch. **44a,** 1063–1078 (1989); received July 25, 1989

The rotational Zeeman effect has been observed in methanimine which was produced from ethylenediamine by flash pyrolysis. The observed vibronic ground state expectation values of the molecular g-values, the magnetic susceptibility anisotropies and the molecular electric quadrupole moments are: $g_{aa} = -1.27099(22)$, $g_{bb} = -0.18975(7)$, $g_{cc} = -0.03440(8)$, $2\xi_{aa} - \xi_{bb} - \xi_{cc} = 12.49(19) \cdot 10^{-6}\,\text{erg}\,\text{G}^{-2}\,\text{mol}^{-1}$, $2\xi_{bb} - \xi_{cc} - \xi_{aa} = 5.22(11) \cdot 10^{-6}\,\text{erg}\,\text{G}^{-2}\,\text{mol}^{-1}$, $Q_{aa} = 0.43(17) \cdot 10^{-26}$ esu cm^2, $Q_{bb} = 1.08(10) \cdot 10^{-26}$ esu cm^2, and $Q_{cc} = -1.51(26) \cdot 10^{-26}$ esu cm^2. With the TZVP ab initio value for the out-off plane electronic second moment as additional input, reliable values can be given also for the individual components of the magnetic susceptibility tensor and for the bulk susceptibility:

$$\xi = (\xi_{aa} + \xi_{bb} + \xi_{cc})/3 = -13.13(88) \cdot 10^{-6}\,\text{erg}\,\text{G}^{-2}\,\text{mol}^{-1}.$$

From low-J a- and b-type zero field transitions the spin-rotation coupling constants and the ^{14}N nuclear quadrupole coupling constants could be redetermined with improved accuracy. These data are compared with our new theoretical results.

Introduction

We have initiated a series of rotational Zeeman effect studies of small imine compounds because of our interest in local additivity rules for the magnetic susceptibility tensor. Such additivity rules have been originally proposed by Benson, Norris, and Flygare [1] by analogy with Pascal's rules for the bulk susceptibilities. Later they were extended by Wiese [2] to include more local subunits. A really reliable local tensor for the imine group is still missing but is of considerable interest for the assessment of nonlocal ring currents in aromatic nitrogen containing heterocycles. Also accurate experimental susceptibilities for small molecules such as methanimine are of special interest for comparison with ab initio values calculated with the IGLO method developed recently by Kutzelnigg and coworkers [3].

The microwave spectrum of methanimine was studied first by Johnson and Lovas [4]. Later Pearson and Lovas [5] devised improved pyrolysis schemes and derived a substitution structure from the rotational constants of six isotopic species. For later use we present their structure in Fig. 1 and Table 1.

The ^{14}N hyperfine interaction including spin-rotation interaction was studied by Brown, Godfrey, and Winkler [6]. In the following we also present an analysis of several low-J zero-field multiplets, where inclusion of b-type transitions leads to improved quadrupole coupling and spin-rotation coupling constants. We then present the analysis of high field molecular Zeeman effect spectra. Next, the molecular electric quadrupole moments and the anisotropies in the second moments of the electronic charge distribution are calculated from the observed Zeeman parameters.

Parallel to the experiments at Kiel extensive ab initio calculations were carried out at Edinburgh. Using the ab initio value for the out-off plane electronic second moment we are in the position to present reliable values for the magnetic susceptibility tensor which are

---

Reprint requests to Prof. Dr. D. H. Sutter, Institut für Physikalische Chemie, Abteilung Chemische Physik, Universität Kiel, Olshausenstr. 40–60, D-2300 Kiel, West Germany.

0932-0784 / 89 / 1100-1063 \$ 01.30/0. – Please order a reprint rather than making your own copy.

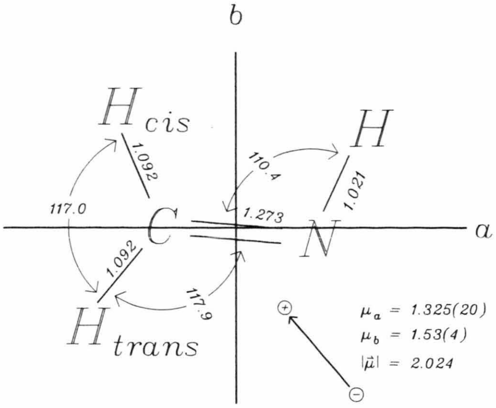

Fig. 1. Microwave substitution structure of methanimine [5a]. Also shown are the principal inertia axes and the orientation of the molecular electric dipole moment [5b].

Table 1. Principal inertia axes coordinates (Å) and rotational constants for CH_2NH [5].

Atom	*a*-coordinate	*b*-coordinate	*c*-coordinate
N	−0.6367	0.0885	0.0000
C	0.6319	−0.0164	0.0000
H_N	−1.0703	−0.8359	0.0000
H_{cis}	1.0617	−1.0203	0.0000
H_{trans}	1.3313	0.8223	0.0000
rotational constants	A_0/MHz 196 211.046(45)	B_0/MHz 34 642.3956(72)	C_0/MHz 29 352.2326(69)

not easily accessible otherwise. This is discussed in the fourth section of the present contribution. In the final section the ab initio work is described in some detail and the calculated results are critically compared to the new experimental data.

Experimental Details

Methanimine was prepared by flash pyrolysis of ethylenediamine in a quartz tube (inner diameter: 1 cm; length: 20 cm) heated to 600°–700 °C:

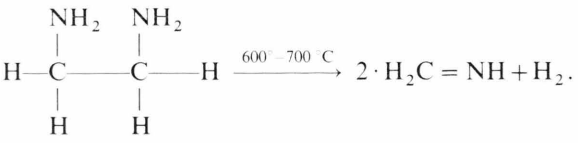

$$\mathrm{H{-}\underset{H}{\overset{NH_2}{C}}{-}\underset{H}{\overset{NH_2}{C}}{-}H} \xrightarrow{600^\circ-700\ ^\circ\mathrm{C}} 2\cdot H_2C=NH+H_2.$$

Since $H_2C=NH$ is unstable in the standard brass waveguide absorption cells (it tends to polymerize at the walls), a flow system was set up. The pyrolysis oven was located as closely as possible to the front end of the absorption cell and the sample was fed coaxially into the cell in order to minimize the number of wall collisions. Typical total pressures were about 10 mTorr at the entrance hole into the cell and about 1 mTorr at the exit slit, i.e. a fairly rapid flow was maintained.

As absorption cells we have used standard *S*-band and *J*-band rectangular waveguide cells (inner cross sections 3.4 cm by 7.2 cm and 1.6 cm by 3.5 cm, respectively), and oversized *X*-band cells (inner cross section: 1 cm by 5 cm). All cells were equipped with a central septum for Stark-effect modulation. The cells could be cooled down to approximately −50 °C by methanol, flowing through a cooling jacket. To record the spectra, a cw microwave spectrometer with phase stabilized backward wave oscillators as radiation sources and square wave Stark-effect modulation was used. In order to reduce modulation broadening we have used a rather low modulation frequency of 8 kHz only. Furthermore, for automatic operation and signal averaging we have used the frequency sweep and data accquisition system developed recently by Stolze [7].

To illustrate the quality of the spectra we present recordings of the 312 ← 313 and 110 ← 111 rotational transitions in Figs. 2 and 3, respectively. The multiplet patterns are mainly caused by the nuclear quadrupole interaction of the ^{14}N nucleus. In Fig. 4 we present the resolved central part of the 110 ← 111 multiplet recorded at a lower total pressure and at a lower power level of the incident microwave radiation. This reduces collision and power broadening at the expense of a decreased signal to noise ratio. The quality of the recording is, however, still sufficient to extract the satellite frequencies with high precission by plotting the sum of the squares of the experimental intensities divided by the sum of the squares of the experimental deviations with respect to height optimized Lorentzians [8] (second trace in Figure 4):

$$P_{\nu_0} = \left\{ \frac{\sum_{\nu=\nu_0-\Delta\nu}^{\nu_0+\Delta\nu} (E_\nu - B_\nu)^2}{\sum_{\nu=\nu_0-\Delta\nu}^{\nu_0+\Delta\nu} (E_\nu - L_\nu)^2} - 1 \right\} \cdot S \tag{1}$$

(E_ν = experimental intensity at frequency point ν; B_ν = baseline value at frequency point ν; L_ν = intensity of Lorentzian centered at frequency ν_0 with least squares optimized height; S = scaling factor for drawing purposes; $2\cdot\Delta\nu$ = frequency window measured in

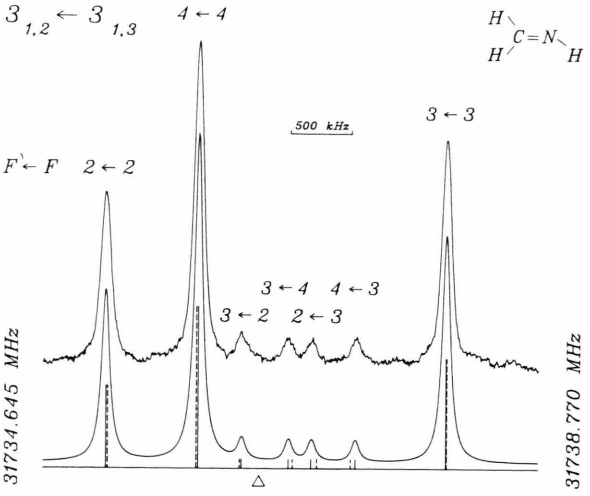

Fig. 2. Recording of the zero field ^{14}N hfs pattern of the $3_{12} \leftarrow 3_{13}$ rotational transition. Lorentzian line shapes with 160 kHz full width at half hight were assumed in the simulation. The dashed pattern was calculated under neglect of spin-rotation.

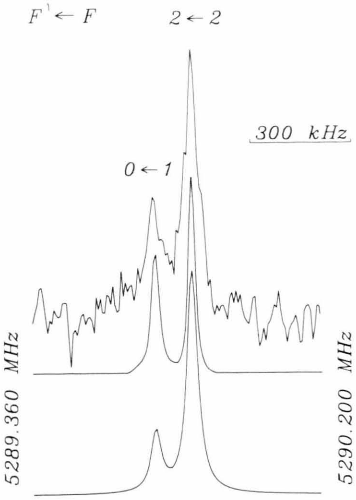

Fig. 4. Central part of the $1_{10} \leftarrow 1_{11}$ ^{14}N hfs pattern recorded at lower pressure and at lower microwave power. The second trace shows the result of our line finder routine described in the Appendix. The bottom trace shows a simulation calculated from the coupling constants presented in Table 4. Lorentzian line profiles were assumed with 80 kHz full width at half height.

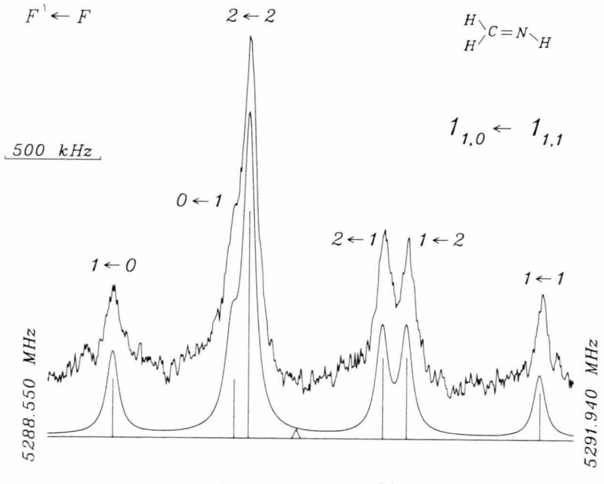

Fig. 3. Recording of the zero field ^{14}N hfs pattern of the $1_{10} \leftarrow 1_{11}$ rotational transition of methanimine. The lower trace was calculated from our ^{14}N quadrupole coupling constants and spin rotation coupling constants presented in Table 4. Lorentzian line shapes with 160 kHz full width at half height were assumed in this simulation.

steps of the digital sweep (for the window width we typically use $2 \cdot \Delta \nu = 3/2$ full linewidth at half height)).

As is shown in the Appendix, the peak heights in such a plot should be roughly proportional to the logarithm of the quotient of the probability that there is a line divided by the probability that there is no line. We note that the experimental splitting between the two $F' \leftarrow F$ satellites obtained that way coincides to better than 100 Hz with the splitting calculated from the optimized quadrupole coupling constants and spin-rotation coupling constants listed below in Table 4.

For the Zeeman studies the absorption cells were located in the gap of a powerful electromagnet. This system has been described in detail in [9] and [10]. Since the microwave radiation is polarized perpendicular to the broad face of the waveguide cells, pure σ- or pure π-type Zeeman spectra can be easily obtained by the appropriate choice of the orientation of the waveguide cells with respect to the exterior field. Due to the increased gap widths necessary to house the oversized cells, maximum field strengths were reduced to about 18 kG. Also the long term fluctuations of the field were slightly higher than previously reported (±5 G rather than ±1 G reported in ref. [9]). This adds 0.03% to the uncertainties of the g-tensor elements and 0.06% to the uncertainties in the measured susceptibility anisotropies (see below).

Analysis of the Zero Field Multiplets

We have recorded and analyzed the zero field hfs multiplets of five low-J rotational transitions, two

Table 2. Hyperfine muliplets of some low-J rotational transitions of $CH_2{}^{14}N$. The splittings are caused by ^{14}N quadrupole coupling and, to a lesser extend, by ^{14}N spin-rotation interaction. The calculated splittings follow from the optimized coupling constants given in Table 4 ($\Delta = \Delta\nu_{exp} - \Delta\nu_{calc}$).

$J'_{K'_a K'_c} - J_{K_a K_c}$ center [MHz]	$F' - F$	Relative intensity	$\Delta\nu_{exp}$ [MHz]	$\Delta\nu_{calc}$ [MHz]	Δ [kHz]
$1_{10} - 1_{11}$	$2-2$	41.70	-0.309	-0.309	0
	$1-1$	8.33	1.558	1.559	-1
5 290.124	$2-1$	13.90	0.547	0.548	-1
	$1-2$	13.90	0.704	0.702	2
	$0-1$	11.10	-1.162	-1.160	-2
	$1-0$	11.10	-0.412	-0.415	3
$2_{11} - 2_{12}$	$3-3$	41.50	-0.439	-0.438	-1
	$2-2$	23.10	1.559	1.559	0
15 869.888	$1-1$	15.00	-1.575	-1.575	0
	$3-2$	5.19	0.754	0.747	7
	$2-3$	5.19	0.373	0.374	-1
	$2-1$	5.00	-0.205	-0.210	5
	$1-2$	5.00	0.192	0.194	-2
$1_{11} - 2_{02}$	$2-3$	46.60	0.078	0.079	-1
	$1-2$	25.00	-0.436	-0.437	1
33 704.854	$2-2$	8.33	0.420	0.420	0
	$1-1$	8.33	-0.934	-0.934	0
	$0-1$	11.10	1.041	1.040	1
$3_{12} - 3_{13}$	$4-4$	40.20	-0.509	-0.509	0
	$3-3$	28.00	1.559	1.558	1
31 736.419	$2-2$	21.20	-1.267	-1.266	-1
	$4-3$	2.68	0.800	0.800	0
	$3-4$	2.68	0.249	0.250	-1
	$3-2$	2.65	-0.151	-0.149	-2
	$2-3$	2.65	0.441	0.441	0
$3_{03} - 2_{12}$	$4-3$	42.90	-0.168	-0.167	-1
	$3-2$	29.60	0.610	0.611	-1
35 065.703	$2-1$	20.00	-0.646	-0.648	2
	$3-3$	3.70	-0.570	-0.574	4
	$2-2$	3.70	1.119	1.120	-1

b-type transitions where the b-component of the molecular electric dipole moment serves as the lever to change the rotational states, and three a-type transitions. Our results are presented in Table 2.

For the analysis of the splittings we have used the standard rigid rotor Hamiltonian supplemented by the ^{14}N nuclear quadrupole coupling interaction which accounts for the potential energy of the electric quadrupole moment of the spinning nucleus within the intramolecular electric field, and by the ^{14}N spin-rotation interaction which accounts for the potential energy of the nuclear magnetic dipole moment in the magnetic field generated by the overall rotation of the molecular charge distribution. This Hamiltonian is given by

$$\hat{\mathscr{H}}_{eff} = \hat{\mathscr{H}}_{rot} + \hat{\mathscr{H}}_{nq} + \hat{\mathscr{H}}_{sr} \tag{2}$$

with $\hat{\mathscr{H}}_{rot}$ the rigid rotor energy, $\hat{\mathscr{H}}_{nq}$ the ^{14}N nuclear quadrupole interaction energy, and $\hat{\mathscr{H}}_{sr}$ the ^{14}N spin rotation interaction energy.

If one sets up the Hamiltonian matrix with respect to the coupled basis, $|J, K_a K_c, I, F, M_F\rangle$, corresponding to the vector coupling scheme $\boldsymbol{F} = \boldsymbol{J} + \boldsymbol{I}$, and if all matrix elements which are off-diagonal in the quantum number J are neglected (an excellent approximation in our present application), then the energy levels corresponding to (2) are given by

$$\begin{aligned}
&\langle J, K_a K_c, I, F, M_F|\, \hat{\mathscr{H}}_{eff}\, |J, K_a K_c, I, F, M_F\rangle \\
&\quad = h\{B_a \langle \hat{J}_a^2\rangle + B_b \langle \hat{J}_b^2\rangle + B_c \langle \hat{J}_c^2\rangle\} \\
&\quad + \frac{\frac{3}{4} C_F(C_F+1) - J(J+1)\, I(I+1)}{J(2J-1)\, I(2I-1)\,(J+1)(2J+3)}\, |e| \\
&\quad \cdot Q_N \sum_g^{g=a,b,c} \left\langle \frac{\partial^2 V}{\partial g^2} \right\rangle \langle \hat{J}_g^2 \rangle \\
&\quad - \frac{h}{2}\, \frac{F(F+1) - I(I+1) - J(J+1)}{J(J+1)} \sum_g^{g=a,b,c} M_{gg} \langle \hat{J}_g^2 \rangle
\end{aligned} \tag{3}$$

with $C_F = F(F+1) - J(J+1) - I(I+1)$.

The other symbols have the following meaning: h = Planck's constant; B_a, B_b, B_c = rotational constants in frequency units; $\langle \hat{J}_a^2\rangle$, $\langle \hat{J}_b^2\rangle$, $\langle \hat{J}_c^2\rangle$ = asymmetric top expectation values for the squares of the angular momentum operators (in units of $\hbar^2$) with respect to the principal inertia axes; e = proton charge; Q_N = nuclear quadrupole moment of the ^{14}N nucleus; $\langle \partial^2 V/\partial a^2\rangle$ etc. are the vibronic ground state expectation values for the second derivatives of the intramolecular Coulomb potential taken at the position of the nitrogen nucleus; M_{aa} etc. are elements of the spin-rotation coupling tensor; $I = 1$ = spin quantum number of the nitrogen spin; J = angular momentum quantum number for the molecular rotation. (Compare (9.75) of [11] for the quadrupole interaction and (9.146) and (9.147) for the spin-rotation interaction, but note that here we follow Flygare's convention [12], [13] for the sign of the spin-rotation interaction.) For completeness we give the rigid rotor angular momentum expectation values of interest here in Table 3. They were calculated by partial differentiation of the rigid rotor energies with respect to the rotational constants as described in [10].

We have also calculated the energy levels by the program described in [14]. In this program the complete Hamiltonian matrix is set up in the coupled basis

Table 3. Expectation values for the squares of the rigid rotor angular momentum components calculated by the Hellmann-Feynman theorem from the rigid rotor energies.

Energy level	$\langle J_a^2 \rangle$	$\langle J_b^2 \rangle$	$\langle J_c^2 \rangle$
1_{11}	1.000000	0.000000	1.000000
1_{10}	1.000000	1.000000	0.000000
2_{02}	0.000778	2.951307	3.047915
2_{12}	1.000000	1.000000	4.000000
2_{11}	1.000000	4.000000	1.000000
3_{03}	0.003880	5.756915	6.239205
3_{13}	1.000475	2.470103	8.529422
3_{12}	1.000498	8.468997	2.530505

Table 4. ^{14}N quadrupole coupling and spin rotation constants (MHz) of CH_2NH. Uncertainties are one standard deviation from the least squares fit (^{a} from the SCF TZVP wave-functions, ^{b} from INDO/2 p-orbital populations; see text).

Constant	This work	Theoretical	Brown et al. [6]
χ_{aa}	−0.9131(16)	−1.0123 ^{a}	−0.898(8)
χ_{bb}	−2.6688(14)	−2.6670 ^{a}	−2.693(8)
χ_{cc}	3.5819(21)	3.6793 ^{a}	3.591(8)
M_{aa}	−0.0548(8)	−0.0541 ^{b}	−0.0495(47)
M_{bb}	−0.0090(3)	−0.0087 ^{b}	−0.0097(27)
M_{cc}	−0.0009(3)	−0.0070 ^{b}	−0.0012(24)

Table 5. INDO nitrogen p-orbital density matrix elements, $P_{p_a p_a}$, $P_{p_a p_b}$, etc. for CH_2NH used in the calculation of the spin-rotation coupling constants according to (4) of the text.

	p_a	p_b	p_c
p_a	1.2401	0.1906	0.0000
p_b	0.1906	1.3062	0.0000
p_c	0.0000	0.0000	1.0898

and the individual *F*-blocks are diagonalized numerically. The results agree, confirming the approximation which leads to (3).

While the rotational constants were taken from the work of Lovas and Johnson [5a], the quadrupole coupling constants and the spin rotation coupling constants were fitted to the observed splittings by the standard least squares procedure. (Note that from (3) these parameters enter linearly into the theoretical expressions for the splittings.) Our result is presented in Table 4. Also given for comparison are the corresponding values determined earlier by Brown and coworkers [6]. It is interesting to note the improvement in the experimental uncertainties. This probably reflects the fact that only *a*-type transitions have been used in the earlier investigation while our present study uses information from both types of transitions with approximately equal weight.

In the second column of Table 4 we also give our ab initio quadrupole coupling constants and approximate values for the spin rotation constants as predicted from INDO wavefunctions. The ab initio work is discussed below. The spin-rotation coupling constants were calculated according to Flygare's approximate expression (21) in [12]. It reads

$$M_{aa} = \frac{2\,|e|\,\mu_n\,g_N\,B_a}{\hbar\,c} \cdot \sum_{n'}^{\substack{\text{nuclei other}\\ \text{than } ^{14}\text{N}}} Z_{n'} \frac{1}{r^3_{n'N}} \left((b_{n'}-b_N)^2+(c_{n'}-c_N)^2\right) - \frac{4\,|e|\,\mu_n\,g_N\,B_a\,\hbar}{c\,m\,|\Delta E|} \cdot \left\langle \frac{1}{r^3} \right\rangle_{\mathrm{p}} \cdot (P_{bb}+P_{cc}-P_{bb}\cdot P_{cc}+P_{bc}\cdot P_{cb})\,. \tag{4}$$

(and cyclic permutations).

The symbols have the following meanings: μ_n = nuclear magneton; g_N = ^{14}N nuclear *g*-value; $\hbar = h/2\pi$; c=velocity of light (all these constants were taken from the Appendix of ref. [11]). $Z_{n'}$ is the atomic number of the n'-th nucleus other than ^{14}N, $b_{n'}-b_N$ is the difference in the *b*-coordinates of the n'-th nucleus and the nitrogen nucleus etc.; $r_{n'N}$ is the distance between the n'-th nucleus and the ^{14}N nucleus; m is the electron mass; $|\Delta E|$ is an average electron excitation energy; $\langle 1/r^3 \rangle_{\mathrm{p}}$ is the electronic expectation value of $1/r^3$ for an electron in a nitrogen p-orbital, and P_{bb}, P_{bc} etc. are elements of the density matrix defined as

$$P_{bb} = 2 \sum_{j}^{\text{occ. orb.}} l^*_{j\mathrm{p}_b}\, l_{j\mathrm{p}_b}\,; \quad P_{bc} = 2 \sum_{j}^{\text{occ. orb.}} l^*_{j\mathrm{p}_b}\, l_{j\mathrm{p}_c}\,, \tag{5}$$

where $l_{j\mathrm{p}_b}$ is the LCAO-coefficient of the nitrogen p_b-orbital in the *j*-th molecular orbital.

The original parameterization of Pople was used in the INDO program. The microwave structure of Pearson and Lovas (see Fig. 1 and Table 1) was used as input for the INDO program and for the calculation of the nuclear contribution to the spin-rotation coupling. The part of the INDO density matrix which is of interest here is given in Table 5. Then with $|\Delta E|$ = 5.4 eV (see [15]) and with $\langle 1/r^3 \rangle = 16.6 \cdot 10^{24}$ cm^2 [16], the values listed in column 2 of Table 4 are predicted for the spin-rotation coupling constants. In view of the crude approximations involved in the derivation of (4), the agreement between our experimental values and the predicted values is remarkably good.

Analysis of the Zeeman-hfs Multiplets

We have studied the Zeeman-hfs multiplets of all five low-J transitions. For the analysis of the splittings we have used the effective Hamiltonian

$$\hat{\mathscr{H}}_{\text{eff}} = \hat{\mathscr{H}}_{\text{rot}} + \hat{\mathscr{H}}_{\text{nq}} + \hat{\mathscr{H}}_{\text{sr}} + \hat{\mathscr{H}}_{\text{nz}} + \hat{\mathscr{H}}_{\text{g}} + \hat{\mathscr{H}}_{\xi}\,. \tag{6}$$

(A detailed description of the theoretical background is given in [10].)

In (6) $\hat{\mathscr{H}}_{\text{nz}}$ represents the nuclear Zeeman effect of the nitrogen nucleus. $\hat{\mathscr{H}}_{\text{g}}$ represents the so called first order rotational Zeeman effect. (It arises from the interaction of the magnetic dipole moment caused by the overall rotation of the molecular charge distribution with the exterior magnetic field.) $\hat{\mathscr{H}}_{\xi}$ represents the second order rotational Zeeman effect. (It arises from the interaction of the field induced intramolecular electronic ring currents with the exterior field.)

Since the exterior field effectively uncouples nitrogen spin precession and molecular overall rotation, the uncoupled basis $|J, K_a K_c, M_J, I, M_I\rangle$ is more appropriate. (For a discussion of the transition from the coupled case at low fields to the uncoupled case at high fields compare for instance [17].) Within this uncoupled basis the diagonal matrix elements take the form (7) and (8). The non-vanishing off-diagonal elements are (9) and (10).

$$\begin{aligned}
&\langle J, K_a K_c, M_J, I, M_I|\,\hat{\mathscr{H}}_{\text{eff}}\,|J, K_a K_c, M_J, I, M_I\rangle \\
&\quad = h\sum_g B_g \langle \hat{J}_g^2\rangle + \tfrac{1}{2}C\{J(J+1)-3M_J^2\} \\
&\quad\cdot \{I(I+1)-3M_I^2\} - \frac{M_J\,M_I}{J(J+1)}\sum_g M_{gg}\langle \hat{J}_g^2\rangle \qquad (7)\\
&\quad -\mu_n g_N M_I H_z - \mu_n \frac{M_J H_z}{J(J+1)}\sum_g g_{gg}\langle \hat{J}_g^2\rangle - \frac{1}{2N_{\text{A}}}\xi H_z^2 \\
&\quad + \frac{1}{N_{\text{A}}}\frac{\{J(J+1)-3M_J^2\}}{(2J-1)(2J+3)J(J+1)}\sum_g(\xi_{gg}-\xi)\langle \hat{J}_g^2\rangle H_z^2
\end{aligned}$$

with

$$C = \frac{|e|\cdot Q}{J(2J-1)\,I(2I-1)(J+1)(2J+3)}\sum_g \left\langle \frac{\partial^2 V}{\partial g^2}\right\rangle \langle \hat{J}_g^2\rangle. \tag{8}$$

$$\begin{aligned}
&\langle J, K_a K_c, M_J, I, M_I|\,\hat{\mathscr{H}}_{\text{eff}}\,|J, K_a K_c, M_J\pm 1, M_I\mp 1\rangle \\
&\quad = \tfrac{3}{4}C(2M_J\pm 1)(2M_I\mp 1) \\
&\quad\cdot \{(J(J+1)-M_J(M_J\pm 1))(I(I+1)-M_I(M_I\mp 1))\}^{1/2} \\
&\quad - \frac{\{(J(J+1)-M_J(M_J\pm 1))(I(I+1)+M_I(M_I\mp 1))\}^{1/2}}{2J(J+1)} \\
&\quad\cdot \sum_g M_{gg}\langle \hat{J}_g^2\rangle, \qquad (9)
\end{aligned}$$

$$\begin{aligned}
&\langle J, K_a K_c, M_J, I, M_I|\,\hat{\mathscr{H}}_{\text{eff}}\,|J, K_a K_c, M_J\pm 2, M_I\mp 2\rangle \\
&\quad = \tfrac{3}{4}C\{(J\mp M_J)(J\mp M_J-1)(J\pm M_J+1)(J\pm M_J+2) \\
&\quad\cdot (I\pm M_I)(I\pm M_I-1)(I\mp M_I+1)(I\mp M_I+2)\}^{1/2}. \qquad (10)
\end{aligned}$$

As compared to the corresponding expressions used earlier (see Sutter and Flygare [18]) for the diagonal elements and Sutter [9] for the off-diagonal elements of the nuclear quadrupole coupling), we have extended the expressions to include the spin-rotation interaction of the nitrogen nucleus. In order to obtain the eigenvalues of the effective Hamiltonian, the M_J, M_I-submatrices of rank $(2J+1)(2I+1)$ which correspond to the different $J, K_a K_c$-states were diagonalized numerically. The relative intensities of the satellites were obtained by the corresponding transformation of the direction cosine elements.

Depending on the orientation of the waveguide cell, the Zeeman-hfs multiplets were recorded under the $\Delta M_J = 0$ or $\Delta M_J = \pm 1$ selection rule. For the nitrogen spin the $\Delta M_I = 0$ selection rule applied throughout since the strong field uncoupled spin and overall rotation. Our observed splittings are given in Table 6 (compare too Figure 5).

From a nonlinear iterative least squares fit to the observed multiplets which was carried out similar to the procedure described in ref. [9], the molecular g values and molecular magnetic susceptibility anisotropies presented in Table 7 were obtained. As described in ref. [17] the sign of the molecular g tensor elements could be determined unambiguously from intermediate field multiplet patterns such as shown in Figure 6.

Table 6. Zeeman ^{14}N quadrupole hfs multiplets in CH_2NH observed under selection rules $\Delta M_I=0$ and $\Delta M_J=0$ and $\Delta M_J=\pm 1$, respectively ($\Delta=\Delta\nu_{exp}-\Delta\nu_{calc}$).

$J'_{K'_-K'_+}-J_{K_-K_+}$ center/MHz H/Gauss	ΔM_J	M_I	$M_J'-M_J$		Rel. int.	$\Delta\nu_{exp}$ [MHz]	$\Delta\nu_{calc}$ [MHz]	Δ [kHz]
$1_{10}-1_{11}$		−1	−1	−1	100		−1.387	
						−1.406	−1.406	0
5 290.131		+1	−1	−1	100		−1.425	
17 253.0	0	0	−1	−1	100	−0.455	−0.457	2
		−1	+1	+1	100		0.672	
						0.664	0.664	0
		+1	+1	+1	100		0.656	
		0	+1	+1	100	1.595	1.594	0
		−1	−1	−1	100		−1.526	
						−1.541	−1.544	3
		+1	−1	−1	100		−1.561	
19 348.0	0	0	−1	−1	100	−0.595	−0.596	1
		−1	+1	+1	100		0.779	
						0.772	0.772	0
		+1	+1	+1	100		0.765	
		0	+1	+1	100	1.702	1.703	−1
$2_{11}-2_{12}$		−1	−2	−2	400		−2.402	
						−2.396	−2.396	0
15 869.888		+1	−2	−2	400		−2.389	
15 991.0	0	0	−2	−2	400	−1.049	−1.051	2
		−1	−1	−1	100		−0.705	
						−0.689	−0.690	1
		+1	−1	−1	100		−0.675	
		−1	+1	+1	100		1.181	
						1.203	1.207	−4
		+1	+1	+1	100		1.233	
		−1	+2	+2	400		1.346	
						1.365	1.366	−1
		+1	+2	+2	400		1.379	
		0	+2	+2	400	2.699	2.693	6
19 877.0	0	−1	−2	−2	400		−2.900	
						−2.893	−2.897	4
		+1	−2	−2	400		−2.893	
		0	−2	−2	400		−1.552	
						−1.565	−1.566	1
		0	−1	−1	100		−1.576	
		0	+1	+1	100	0.793	0.790	3
		−1	+1	+1	100		1.434	
						1.460	1.456	4
		+1	+1	+1	100		1.477	
		−1	+2	+2	400		1.772	
						1.790	1.790	0
		+1	+2	+2	400		1.807	
		0	+2	+2	400	3.120	3.120	0
$1_{11}-2_{02}$		0	−1	0	20	−5.650	−5.657	7
33 704.854		−1	−1	0	20		−4.995	
						−5.036	−5.044	8
10 544.0	1	+1	−1	0	20		−5.093	
		−1	0	+1	60		−1.104	
						−1.127	−1.124	−3
		+1	0	+1	60		−1.144	
		0	0	+1	60	−0.435	−0.433	−2
		−1	0	−1	60		0.671	
						0.663	0.661	2
		+1	0	−1	60		0.650	
		0	0	−1	60	1.346	1.343	3
		0	+1	+2	120	3.338	3.343	−5
		−1	+1	+2	120		3.544	
						3.538	3.535	3
		+1	+1	+2	120		3.529	
13 186.0	1	0	−1	0	20	−6.951	−6.955	4
		−1	−1	0	20		−6.297	
						−6.345	−6.342	3
		+1	−1	0	20		−6.386	
		0	−1	−2	120	−4.486	−4.483	−3
		−1	0	+1	60		−1.331	
						−1.349	−1.348	−1
		+1	0	+1	60		−1.366	
		0	0	+1	60	−0.658	−0.656	−2
		−1	0	−1	60		0.890	
						0.883	0.883	0
		+1	0	−1	60		0.876	
		0	0	−1	60	1.568	1.569	−1
		0	+1	+2	120	4.202	4.210	1
		−1	+1	+2	120		4.392	
						4.392	4.391	1
		+1	+1	+2	120		4.390	
		0	+1	0	20	6.199	6.200	−1
		−1	+1	0	20		6.810	
						6.820	6.823	−3
		+1	+1	0	20		6.831	
15 756.0	1	0	−1	−2	120	−5.336	−5.133	−3
		−1	−1	−2	120		−5.122	
						−5.153	−5.155	2
		+1	−1	−2	120		−5.187	
		−1	0	+1	60		−1.551	
						−1.561	−1.566	5
		+1	0	+1	60		−1.581	
		0	0	+1	60	−0.874	−0.874	0
		−1	0	−1	60		1.105	
						1.094	1.100	−6
		+1	0	−1	60		1.094	
		0	0	−1	60	1.785	1.787	−2
		0	+1	+2	120	5.036	5.034	2
		−1	+1	+2	120		5.222	
						5.225	5.223	2
		+1	+1	+2	120		5.224	
		0	0	+1	20	7.488	7.491	−3
$1_{11}-2_{02}$		−1	−1	−1	30		−4.619	
						−4.659	−4.660	1
33 704.874		+1	−1	−1	30		−4.700	
11 678.0	0	−1	0	0	40		−0.170	
						−0.185	−0.185	0
		+1	0	0	40		−0.200	
		0	0	0	40	0.397	0.394	−3
		−1	+1	+1	30		5.030	
						5.030	5.034	−4
		+1	+1	+1	30		5.038	
14 591.0	0	0	−1	−1	30	−6.352	−6.357	5
		−1	−1	−1	30		−5.811	
14 591.0	0					−5.856	−5.849	−7
		+1	−1	−1	30		−5.893	
		0	0	0	40	0.405	0.401	4
19 348.0	0	0	−1	−1	30	−8.297	−8.298	1
		−1	−1	−1	30		−7.755	
						−7.790	−7.789	−1
		+1	+1	+1	30		−7.823	
$3_{12}-3_{13}$		−1	+3	+3	90		2.408	
						2.433	2.435	−2
31 736.426		+1	+3	+3	90		2.461	
17 253.0	0	0	+3	+3	90	3.983	3.977	−5
11 678.0	0	0	−3	−3	90	−1.044	−1.040	−4
$3_{03}-2_{12}$		0	−2	−2	50	3.330	3.330	0
35 065.711		−1	−2	−2	50		2.505	
						2.555	2.552	3
11 678.0	0	+1	−2	−2	50		2.599	
		−1	−1	−1	80		1.418	
						1.467	1.470	−3
		+1	−1	−1	80		1.522	
		0	−1	−1	80	1.215	1.220	−5
		0	0	0	90	−0.344	−0.345	1
		0	+1	+1	80	−1.499	−1.508	9
		0	+2	+2	50	−2.367	−2.369	2
		−1	+2	+2	50		−3.137	
						−3.119	−3.118	−1
		+1	+2	+2	50		−3.100	
17 253.0	0	0	0	0	90	−0.333	−0.337	4
19 248.0	0	0	0	0	90	−0.332	−0.332	0
$3_{03}-2_{12}$		0	−1	−2	20	4.047	4.052	−5
		0	−3	−2	300	2.010	2.008	2
35 065.711		0	0	−1	60	1.983	1.991	−8
		0	+1	0	120	0.487	0.496	−9
10 544.0	1	0	−2	−1	200	0.088	0.098	−10
		0	+2	+1	200	−0.590	−0.593	3
		0	−1	0	120	−1.268	−1.259	9
		0	+3	+2	300	−1.381	−1.385	4
		0	0	+1	60	−2.201	−2.208	7
		−1	−3	−2	300		1.476	
						1.523	1.526	−3
		+1	−3	−2	300		1.575	
		−1	−1	0	120		−0.705	
						−0.669	−0.670	1
		+1	−1	0	120		−0.635	
		−1	+1	0	120		1.042	
						1.080	1.087	−7
		+1	+1	0	120		1.132	
		−1	0	+1	60		−2.142	
						−2.096	−2.097	1
		+1	0	+1	60		−2.052	
		−1	+2	+1	200		−0.298	
						−0.239	−0.245	6
		+1	+2	+1	200		−0.192	
		−1	+3	+2	300		−1.874	
						−1.842	−1.845	3
		+1	+3	+2	300		−1.816	

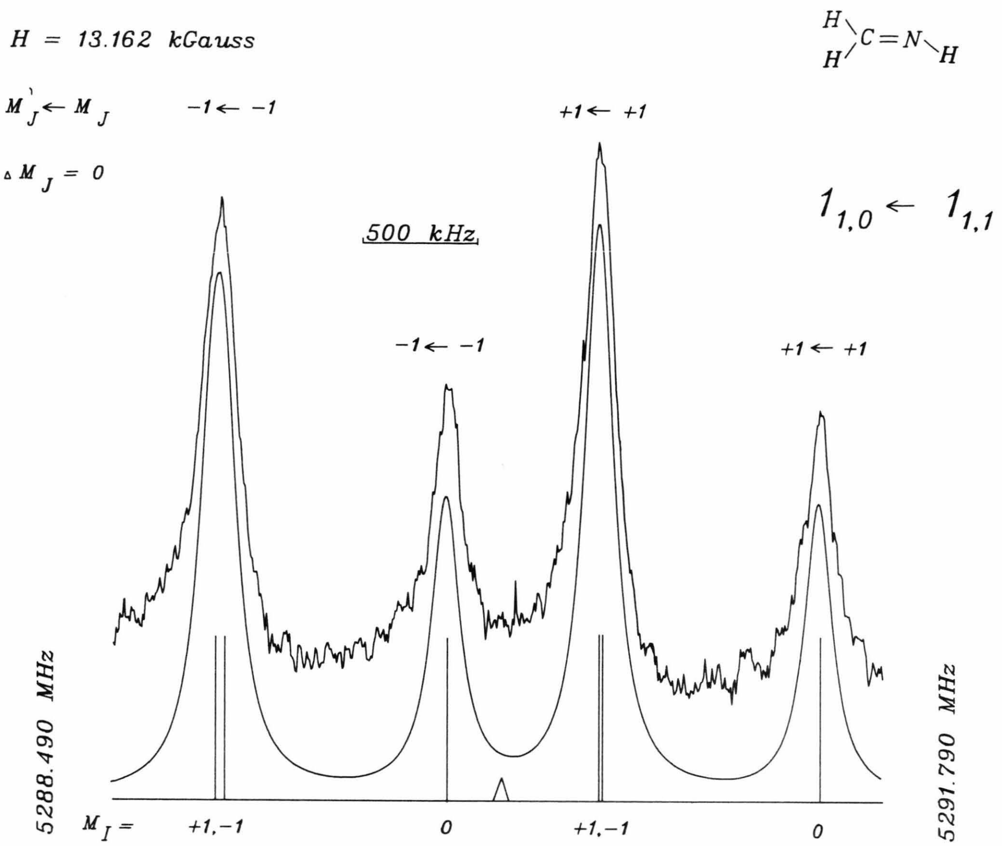

Fig. 5. Zeeman-hfs-multiplet of the 110 ← 111 rotational transition observed under $\Delta M_J = 0$ (and $\Delta M_I = 0$) selection rules. In the absence of ^{14}N quadrupole coupling a doublet of equal intensities would be observed corresponding to the $M_J = 1$ to $M_J = 1$, and $M_J = -1$ to $M_J = -1$ transitions, respectively. ^{14}N quadrupole coupling splits each of these satellites into a triplet corresponding to states with nitrogen spin parallel, perpendicular and antiparallel to the exterior magnetic field.

Table 7. Molecular magnetic g-tensor and anisotropies of the molecular magnetic susceptibility (in units of 10^{-6} erg G^{-2} mol^{-1}) of CH$_2$NH.

Molecular Magnetic g-tensor	g_{aa} g_{bb} g_{cc}	−1.27099(22) −0.18975(7) −0.03440(8)
Magnetic Susceptibility Anisotropy	$2\xi_{aa} - \xi_{bb} - \xi_{cc}$ $2\xi_{bb} - \xi_{aa} - \xi_{cc}$	12.49(19) 5.22(11)

With the theoretical expressions for the g- and ξ-tensor elements

$$g_{aa} = \frac{m_p \cdot 8\pi^2 B_a}{h} \cdot \left\{ \sum_n^{\text{nuclei}} Z_n (b_n^2 + c_n^2) + \frac{2}{m} \sum_v^{\text{ex. states}} \frac{|\langle 0|\mathcal{L}_a|v\rangle|^2}{E_0 - E_v} \right\}, \tag{11}$$

$$\xi_{aa} = -\frac{e^2}{4mc^2} \left\{ \langle 0| \sum_j^{\text{electrons}} (b_j^2 + c_j^2) |0\rangle + \frac{2}{m} \sum_v^{\text{ex. states}} \frac{|\langle 0|\mathcal{L}_a|v\rangle|^2}{E_0 - E_v} \right\}, \tag{12}$$

with m_p = mass of the proton and

$$\mathcal{L}_a = \frac{\hbar}{i} \sum_j^{\text{electrons}} \left(b_j \frac{\partial}{\partial c_j} - c_j \frac{\partial}{\partial b_j} \right) \tag{13}$$

the a-component of the electronic angular momentum operator with respect to the rotating molecular frame, further molecular properties can be determined from the measured Zeeman parameters.

These additional molecular properties include the molecular electric quadrupole moment, the aniso-

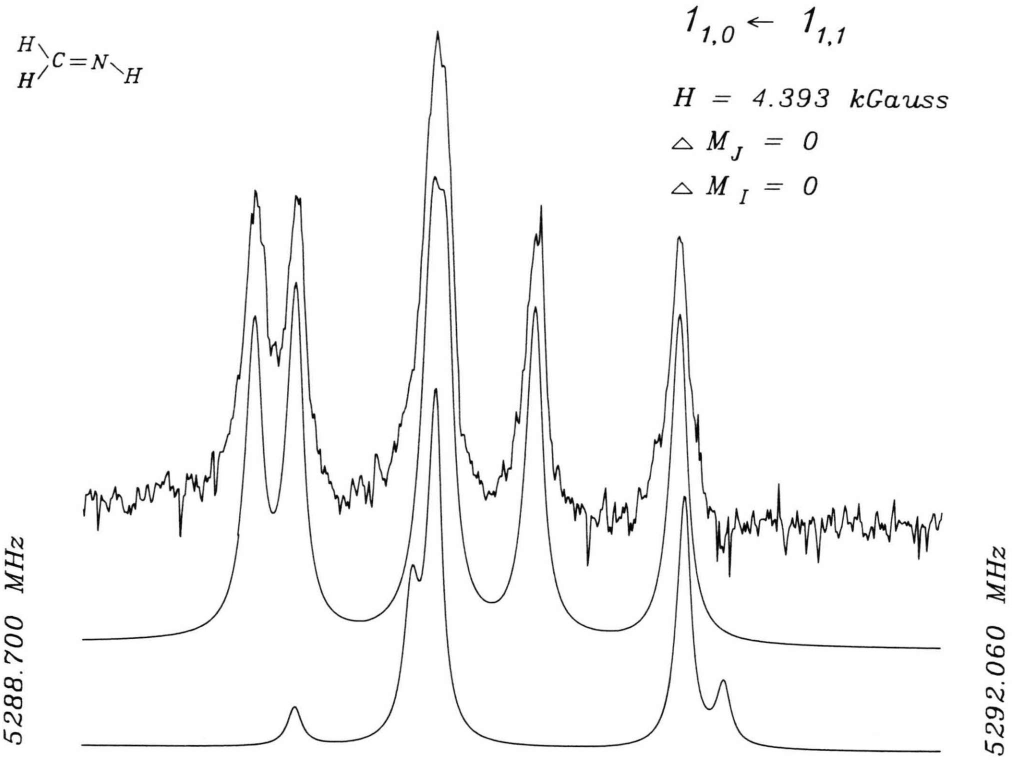

Fig. 6. Intermediate field Zeeman-hfs-multiplet of methanimine. As described in [17], the signs of the molecular g-values can be determined unambiguously from such intermediate field multiplets, while only the relative signs of the g-values can be determined from high field Zeeman spectra. The second trace was calculated with negative g-values. The bottom trace was calculated with positive g-values. The agreement between the experiment and the second trace confirms the choice of signs presented in Table 4.

tropies in the second moments of the electronic charge distribution and – if a value for the bulk susceptibility were available – the second moments of the charge distribution and the diagonal elements of the magnetic susceptibility tensor, all referred to the principal inertia axes coordinate system. (See [19] for the theoretical expressions for the g-values and [20] for the susceptibilities. A combined derivation which starts from the molecular Lagrangian has been presented in [10].)

Molecular Electric Quadrupole Moments and the Anisotropies in the Second Moments of the Electronic Charge Distribution

Molecular electric quadrupole moments play an important role for instance in intermolecular rotational energy transfer in low density gases and in the preorientation of molecules in liquid phase reactions. While they are not easily accessible to experiment otherwise, they can be directly calculated from the rotational constants and the five Zeeman parameters in Table 7 using a general expression derived by Hüttner, Lo, and Flygare [21]:

$$
\begin{aligned}
Q_{aa} &= \frac{|e|}{2}\left\{\sum_{n}^{\text{nuclei}} Z_n(2a_n^2-b_n^2-c_n^2) - \langle 0|\sum_{j}^{\text{electrons}}(2a_j^2-b_j^2-c_j^2)|0\rangle\right\} \\
&= -\frac{h|e|}{16\pi^2 m_\text{p}}\left\{\frac{2g_{aa}}{B_a}-\frac{g_{bb}}{B_b}-\frac{g_{cc}}{B_c}\right\} \\
&\quad -\frac{2mc^2}{|e|N_\text{A}}\{2\xi_{aa}-\xi_{bb}-\xi_{cc}\}\,. \qquad (14)
\end{aligned}
$$

Strictly speaking (14) only applies within the model of a rigid nuclear frame. However Sutter and Flygare [10] have presented arguments which show that

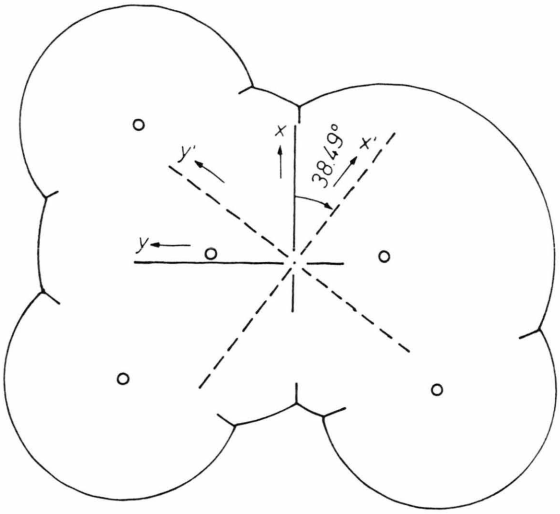

$Q_{x'x'} = +4.041 \cdot 10^{-26}$ esu cm^2
$Q_{y'y'} = -2.424 \cdot 10^{-26}$ esu cm^2

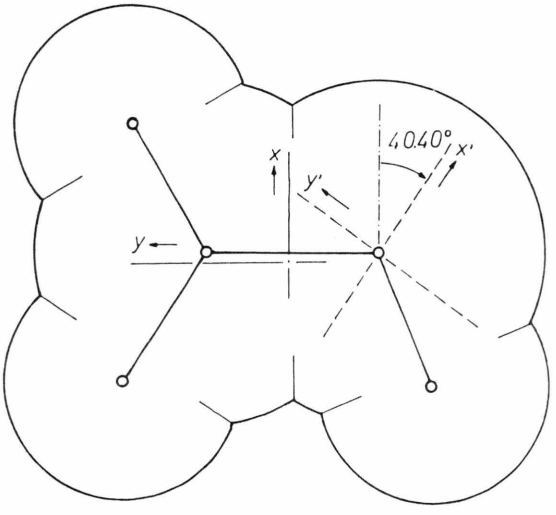

$\chi_{y'y'} = +0.792$ MHz $\chi_{x'x'} = -4.471$ MHz

Fig. 7. Orientation of the molecular electric quadrupole moment tensor and of the ^{14}N nuclear quadrupole coupling tenor in methanimine as calculated from the TZVP wavefunction. Note that the quadrupole moment is given with respect to the nuclear center of charge (x-axis perpendicular to the C=N bond), which is located at $a_{ncc} = 0.0824$ Å and $b_{ncc} = -0.0601$ Å with respect to the principal inertia axes system of the microwave r_s-structure (see Table 1). Transformation into the principal inertia axes system requires the knowledge of the components of the molecular electric dipole moment (see [5b]).

quadrupole moments calculated from (14) should come close to vibronic ground state expectation values for all molecules which undergo only small amplitude vibrations. (Deviations from this general rule have been discussed for instance by Engelbrecht and Sutter for the case of low barrier internal rotations [22] and by Perry and Moss [23] for the case of large amplitude bending vibrations.)

Our experimental quadrupole moments calculated according to (14) are given in Table 8. Also given for comparison are the quadrupole moments calculated from INDO wavefunctions by the method of Hamer, Engelbrecht, and Sutter [24], and our new ab initio results calculated at Edinburgh with a triple zeta valence basis with polarization functions involving 58 gaussian type orbitals (TZVP).

The five Zeeman parameters together with the molecular structure and the rotational constants can also be used to calculate experimental values for the anisotropies in the second moments of the electronic charge distribution. The second moments are defined as

$$\langle a^2 \rangle = \langle 0 | \sum_{j}^{\text{electrons}} a_j^2 | 0 \rangle . \tag{15}$$

Comparison with the theoretical expressions given in (11) and (12) leads to the following expressions for the anisotropies:

$$\begin{aligned} &\langle 0 | \sum_{j}^{\text{electrons}} (a_j^2 - b_j^2) | 0 \rangle \\ &= \sum_{n}^{\text{nuclei}} Z_n (a_n^2 - b_n^2) + \frac{h}{8\pi^2 m_{\text{p}}} \left(\frac{g_{aa}}{B_a} - \frac{g_{bb}}{B_b} \right) \qquad (16) \\ &+ \frac{4 m c^2}{3 e^2 N_{\text{A}}} \{ (2\xi_{aa} - \xi_{cc} - \xi_{cc}) - (2\xi_{bb} - \xi_{cc} - \xi_{aa}) \} \end{aligned}$$

(and cyclic permutations).

Just as is the case with the molecular electric quadrupole moments, the "experimental" anisotropies derived from the Zeeman parameters can be used as a further test for the quality of ab initio wavefunctions in the outer regions of the molecule. In Table 8 we list our experimental results together with our new theoretical values.

Diagonal Elements of the Magnetic Susceptibility Tensor and the Individual Second Moments of the Electronic Charge Distribution

Additional input is needed if one is interested in the individual magnetic susceptibility tensor elements and

Table 8. Comparison of the experimental molecular electric quadrupole moments (see (14)) and the anisotropies in the second moments of the electronic charge distributions (see (16)) with the corresponding theoretical values. The second moments for the nuclear charge distribution are calculated from the microwave structure as $\sum_n Z_n \cdot a_n^2 = 9.279(11)$ Å^2 and $\sum_n Z_n \cdot b_n^2 = 2.472(7)$ Å^2. Here the uncertainties follow by gaussian error propagation from the uncertainties in the bond distances and bond angles quoted in Table V of [5]. (Q_{ab}(TZVP-SCF) $= 3.2251 \cdot 10^{-26}$ esu cm^2).

	Experimental	INDO	TZVP-SCF (r_e)
$Q_{aa}/10^{-26}$ esu cm^2	0.43(17)	0.04	0.5896
$Q_{bb}/10^{-26}$ esu cm^2	1.08(10)	1.07	1.0279
$Q_{cc}/10^{-26}$ esu cm^2	−1.51(26)	−1.11	−1.6175
$\langle\lvert\sum a_i^2 - b_i^2\rvert\rangle/$Å^2	6.91(20)	6.96	6.6647
$\langle\lvert\sum b_i^2 - c_i^2\rvert\rangle/$Å^2	2.12(13)	2.17	2.0395
$\langle\lvert\sum c_i^2 - a_i^2\rvert\rangle/$Å^2	−9.03(14)	−9.12	−8.7042

second moments of the electronic charge distribution. The standard input here would be an experimental value for the bulk susceptibility

$$\xi = (\xi_{aa} + \xi_{bb} + \xi_{cc})/3 \,.$$

In our case, however, the experimental determination of the bulk susceptibility would be difficult due to the high reactivity of the compound. As a different approach we have therefore used our most reliable ab initio value for $\langle c^2 \rangle$, i.e. the one calculated by the Hartree Fock SCF method with the TZVP basis. This value is $\langle c^2 \rangle = 2.854 \cdot 10^{-16}$ cm^2. (The TZV-basis leads to a slightly larger value: $\langle c^2 \rangle = 2.880 \cdot 10^{-16}$ cm^2 while estimates from additivity rules derived by Blickensderfer, Wang, and Flygare [25] on one hand and by Maksic and Mikac [26] on the other hand lead to $\langle c^2 \rangle$ values of $2.75 \cdot 10^{-16}$ cm^2 and $2.60 \cdot 10^{-16}$ cm^2, respectively).

Now from the theoretical expressions for the g- and ξ-tensor elements reported in (12) and (13) $\langle c^2 \rangle$ is related to the g- and ξ-tensor elements:

$$\langle c^2 \rangle = \frac{2mc^2}{e^2 N_A} (\xi_{cc} - \xi_{aa} - \xi_{bb}) + \frac{h}{16\pi^2 m_p} \left(\frac{g_{cc}}{B_c} - \frac{g_{aa}}{B_a} - \frac{g_{bb}}{B_b} \right). \tag{17}$$

If this equation is solved for $(\xi_{cc} - \xi_{aa} - \xi_{bb})$ with the experimental g-values, the rotational constants and the TZVP-value for $\langle c^2 \rangle$ as input data, and if the result is combined with the experimental susceptibility anisotropies from Table 7, the individual components of the magnetic susceptibility tensor as well as the bulk susceptibility are calculated in units of 10^{-6} erg G^{-2} mol^{-1} as

$$\xi_{aa} = -\ 8.91(86), \quad \xi_{bb} = -11.42(87),$$
$$\xi_{cc} = -19.07(91), \quad \xi \ = -13.13(88).$$

The uncertainties follow by Gaussian error propagation from a very conservative $\pm 0.1 \cdot 10^{-16}$ cm^2 estimate for the uncertainty in the ab initio value of $\langle c^2 \rangle$ and from the experimental uncertainties in the Zeeman parameter listed in Table 7.

Now from cyclic permutations of (17) we can also calculate the values for the other electronic second moments. The result in units of 10^{-16} cm^2 is

$$\langle a^2 \rangle = 11.89(14), \quad \langle b^2 \rangle = 4.97(13).$$

The uncertainties follow from the estimated $\pm 0.1 \cdot 10^{-16}$ cm^2 uncertainty in the ab initio value for $\langle c^2 \rangle$, from the experimental uncertainties in the Zeeman parameters, and from the uncertainties in the geometry of the nuclear frame, respectively.

From the anisotropies in the local (atom) susceptibility deduced from Table II.2 of [10] (all values in units of 10^{-6} erg G^{-2} mol^{-1})

$$\Delta\xi(\mathrm{H}-) \ = \xi_\perp(\mathrm{H}-) \ - \xi_\parallel(\mathrm{H}-) \ = -0.455,$$
$$\Delta\xi(>\mathrm{C}=) = \xi_\perp(>\mathrm{C}=) - \xi_\parallel(>\mathrm{C}=) = -3.635$$

($\xi_\perp$ denotes the out-off plane susceptibility and $\xi_\parallel$ the average in-plane susceptibility), and from our experimental value:

$$\Delta\xi(\mathrm{H_2C{=}NH}) = \xi_{cc} - (\xi_{aa} + \xi_{bb})/2 = -8.855\,,$$

a preliminary value for the local contribution of the imine nitrogen to the out-off plane minus average in-plane susceptibility follows as

$$\Delta\xi(=\mathrm{N}') = \Delta\xi(\mathrm{H_2C{=}NH}) - 3\Delta\xi(\mathrm{H}-) - \xi(>\mathrm{C}=)$$
$$= -3.855,$$

i.e. close to the currently accepted value for a sp^2 hybridized carbon atom.

To broaden the experimental basis for this increment and for the assessment of neighbouring bond effects we are currently investigating the rotational Zeeman effect of several other small open chain molecules containing the imine group.

Table 9. Ab initio equilibrium structures (r_e) as a function of basis set.

Basis set		Bond distances (Å)				Bond angles (deg.)			
Name	GTO's	CH_{trans}	CHC	CN	NH	NCH_{trans}	NCH_{cis}	CNH	HCH
STO-3G	13	1.0889	1.0908	1.2728	1.0403	119.1	125.5	109.1	115.4
SV	24	1.0731	1.0803	1.2719	1.0085	118.7	124.7	116.0	115.4
DZ	26	1.0866	1.0926	1.2416	1.0190	118.9	124.7	115.2	116.4
DZD	38 [c]	1.0943	1.0980	1.2560	1.0144	119.1	124.8	111.0	116.1
TZV	37	1.0730	1.0794	1.2605	1.0086	118.9	124.4	115.7	116.7
TZVP	58	1.0795	1.0837	1.2476	1.0040	119.2	124.4	111.9	116.7
MP3/6-31G**	45 [a]	1.085	1.089	1.274	1.020	118.7	125.1	109.7	116.2
DZ-CAS	26 [b]	1.1082	1.0897	1.3191	1.0221	117.8	124.8	112.8	117.4
DZDCAS	38 [b, c]	1.1124	1.0949	1.2944	1.0160	118.3	124.7	109.4	116.2
Microwave	–	1.0920	1.0920	1.2729	1.0210	117.9	125.1	110.4	117.0

[a] M. Rodler, R. D. Brown, P. D. Godfrey, and B. Kleibömer, J. Molec. Spectrosc. **118,** 267 (1986).
[b] Multiconfiguration SCF (1292 configurations with 6 electrons distributed in 9 MOs).
[c] As for DZ, but with d-orbitals on C and N with exponents 0.6 and 0.8, respectively.

Theoretical Studies

a) Equilibrium Structures

The equilibrium structure (r_e) of methanimine was sought using the ab initio gradient technique of the GAMESS suite of programs [27], mounted at the ULCC Cray-1s computer. A series of gaussian type orbital bases (GTOs) varying from 13 to 58 were used, and in the first stage r_e was calculated with single configuration SCF methods. In a subsequent stage, a multi-configuration SCF (complete active space, CASSCF) was used with two medium sized bases. The full results are shown in Table 9. The wave functions of the largest pair of single configuration SCF studies (TZVP, triple zeta valence + polarization) were refined by all valence electron configuration interaction, to determine the effect upon the molecular properties obtained.

b) Molecular Properties Derived from the Wave-Functions

In principle conversion of the theoretical field gradients to experimental quadrupole coupling constants (MHz) requires knowledge of the ^{14}N nuclear quadrupole moment (Q_N). In practice, due to the limited precission in the wave-functions, the Q_N value is better regarded as a conversion factor which is both basis set and method dependent (i.e. SCF, MC-SCF, CI). For the DZ basis we have used −3.5244 MHz/a.u. as conversion factor [28, 29]. For the TZVP basis we have insufficient data to allow a linear correlation with experiment, so that the values based on theoretical data for ammonia were utilized. The experimental value for the quadrupole coupling constant in NH_3 is −4.08923 MHz [30] and hence allowed the evaluation of Q_N at the SCF, MC-SCF (CASSCF), CI levels. For the TZVP basis our conversion factor determined that way is −4.0111 MHz/a.u. A remaining problem in relating the theoretical to experimental data lies with the structure. Strictly the theoretical data must be evaluated at the r_e structure, and this has been done in Table 10, but with a comparison of the TZVP data at the r_s structure. In the latter case the change from r_e to r_s leads to a slight drop of all tensor elements (ca. 2–5%). These changes indicate that the remaining discrepancies between the ab initio values and the experimental results may be largely due to the neglect of vibrational averaging in the former values.

In Table 11 we give the theoretical values of the molecular electric quadrupole moment and other second moments of the charge distribution, with both nuclear and electronic contributions to the tensor elements. The data labeled x, y, z give values in the nuclear center of charge system. It refers to the r_e TZVP/DZ structures. The y-axis was chosen to be parallel to the N=C internuclear axis, and the x-axis was chosen to point to the side of the single hydrogen atom. The z- and c-axes are parallel and perpendicular to the molecular plane. The diagonalized quadrupole moment tensor axes (x', y', z) make an angle $\sphericalangle(x, x')$ of 38.49° to (x, y, z), while the $\sphericalangle(y, a)$ angle is −4.57°.

Table 10. Ab initio ^{14}N nuclear quadrupole coupling constants in methanimine. Our experimental values, which are effectively vibronic ground state expectation values, are also given for direct comparison. At the bottom we give values with respect to the (x, y, z)-system (y-axis along the NC-bond pointing from N to C, z-axis out-off plane, x-axis perpendicular to the NC-internuclear axis and pointing to the side of the single hydrogen atom). The principal x' axis of the coupling tensor makes angles $\sphericalangle(x, x') = -40.40°$ (SCF) and $-39.91°$ (CI), respectively. (χ_{aa} and χ_{bb} are not given in [32]. The values in brackets were calculated from the quoted values $\chi_{x'x'} = -4.86$ MHz and $\chi_{y'y'} = +1.24$ MHz assuming $\sphericalangle a x' = 54.16°$).

Method	Basis	χ_{aa}/MHz	χ_{bb}/MHz	χ_{cc} MHz	Ref.
SCF	13	(−0.85)	(−2.77)	3.62	[32]
SCF (r_s)	58	−0.9988	−2.5511	3.5498	this work
SCF (r_e)	58	−1.0123	−2.6670	3.6793	this work
MC-SCF (r_e)	58	−0.8736	−2.5310	3.4047	this work
CI (r_e)	58	−0.8819	−2.5126	3.3945	this work
Microwave		−0.9131(16)	−2.6688(14)	3.5819(21)	this work

		χ_{xx}/MHz	χ_{yy}/MHz	χ_{zz}/MHz	χ_{xy}/MHz	
SCF (r_e)	58	−2.2599	−1.4194	3.6793	2.5976	this work
CI (r_e)	58	−2.0776	−1.1939	3.2715	2.4597	this work

Table 11. TZVP-SCF-values (58 GTO's) for the second moments (in units of 10^{-16} cm^2) and the molecular electric quadrupole moments (in units of 10^{-26} esu cm^2), calculated at the r_e-structure. Values labelled x', y', z' refer to the diagonalized system (compare too Figure 7). Shorthands used: $x^2_{\text{nuclear}} = \sum_{n}^{\text{nuclei}} Z_n x_n^2$ and $x^2_{\text{electronic}} = -\langle 0| \sum_{j}^{\text{electrons}} x_j^2 |0\rangle$ etc.

	x^2	y^2	z^2	xy	x'^2	y'^2
Nuclear	2.5145	8.9027	0	0.9345	5.8994	5.5178
Electronic	−4.9307	−11.5211	−2.8539	−0.4974	−7.9680	−8.4838
Total	−2.4162	−2.6184	−2.8539	0.4371	−2.0686	−2.9660

	Q_{xx}	Q_{yy}	Q_{zz}	Q_{xy}	$Q_{x'x'}$	$Q_{y'y'}$	$Q_{z'z'}$
Nuclear	−9.3023	36.7197	−27.4174	6.7323	15.0833	12.3341	−27.4174
Electronic	10.8394	−36.6393	25.8000	−3.5830	−11.0422	−14.7578	25.8000
Total	1.5371	0.0804	−1.6174	3.1493	4.0412	−2.4237	−1.6174

Footnote: The conversion factors from atomic to cgs units are 1 au $\triangleq 0.2800 \cdot 10^{-16}$ esu cm^2 for the second moments and 1 au $\triangleq 1.3450 \cdot 10^{-26}$ esu cm^2 for the quadrupole moments.

c) Discussion of the Structure of Methanimine

At first sight the structures (Table 9) obtained appear very similar, and largely independent of basis set. However there are certain trends which have more general importance. The TZVP basis set calculation is the largest yet reported for this molecule, and has the lowest energy (SCF: −94.0642 a.u.; CI: −94.3759 a.u.), to be compared with that from an MP3/6-31 G** basis (−94.3570 a.u.) [31]. The last calculation has Möller-Plesset corrections to the SCF wave-function (effectively SV + polarization) to third order and is the only previous r_e structure calculated with methods beyond the single configuration SCF. As the basis set increases there is a slight shortening of the CN distance below that from the r_s structure, although the CNH-angle comes closer to the r_s-value in this sequence. The smallest (STO-3 G) basis gives a fortuitiously good agreement of r_e with r_s, but the wavefunction is so restricted that electronic properties cannot be well determined from it. It thus appears that polarization functions (DZ versus DZP, TZV versus TZVP) whilst correcting the difference in CNH overshorten CN. The reason appears to be an inadequate representation of the π-MOs in the ground state. Clearly incorporation of the antibonding CN* into the wave-function can be expected to increase the CN length, and this is found in an extreme form when comparing DZ with DZ-CAS. When polarization is introduced as in DZD (d-orbitals on C and N) or in the MP3/6-31 G** (d-orbitals on C and N, and p-orbitals on H), both the CN and CNH parameters improve. Although the TZVP MC-SCF calculation contained some 35585 configurations, the wave-function is very well represented by the following equation, where ψ_0 is the single configuration SCF and ψ_1 that obtained by double replacement of the 1a″ by 2a″:

$$\psi_{\mathrm{MCSCF}}^{\mathrm{TZVP}} = 0.965\,\psi_0 - 0.148\,\psi_1\,.$$

(The MO's 1a″ and 2a″ are the CN π-bonding and π^*-antibonding orbitals, respectively).

Comparison of the DZD-CASSCF result with the DZD one alone (DZ plus d-orbitals on C, N) shows that CNH is further corrected relative to the microwave r_s structure, and whilst the CN length is now shorter it is still slightly long. We may note that we consider the MP3/6-31 G** result, which used basically the split-valence (SV) basis with polarization on H, N and C, as slightly fortuitious, since a feature of the MPn corrections is that they are not stable in predictions with small n.

d) ^{14}N Nuclear Quadrupole Coupling

The values in the nuclear center of charge coordinate system (y-axis parallel to N=C) and inertia axes data are given in Table 10. The effects of CI are small as noted above, but the agreement with the microwave data is slightly improved by MC-SCF/CI at the TZVP level. The present values of the diagonalized tensor show a high value in the general direction of the N lone pair axis, making an angle of about 49° with the N=C bond. This is in line with some earlier calculations which are collected in [32]. These calculations also show that minimal basis sets cannot yield the correct balance between σ- and π-tensor elements [32].

e) Second Moments

The theoretical (TZVP) data in the nuclear center of charge system (x, y, z) and in the diagonalized system (x', y', z) are shown in Table 11, with the corresponding inertial axis data in Table 8. The present definition of terms leads to the total of any element being the sum of nuclear and electronic terms. When the electronic terms are separated and the anisotropy of the second moments obtained (Table 8), it is seen that the TZVP and INDO basis results are both in good agreement with the experimental values derived from the Zeeman data. The "good" result of the INDO calculation is however fortuitious since $\langle a^2\rangle$-INDO, $\langle b^2\rangle$-INDO, and $\langle c^2\rangle$-INDO are all three low by approximately the same amount, and this error largely cancels in the differences. We may note, however, that a previous study [33] indicated that quite in general theoretical values for the anisotropies of the second electronic moments are not critically dependent upon the method of calculation.

Acknowledgements

The Kiel group gratefully acknowledges the financial support by Deutsche Forschungsgemeinschaft and Fonds der Deutschen Chemischen Industrie.

Appendix

The Theory Behind the Line Finder Routine

The theory behind (1) of the text (compare with Fig. 4) which was used to find the correct frequencies also in comparatively noisy experimental spectra is based on the assumption of a gaussian noise distribution, i.e. the probability that the noise voltage at the input of the analog to digital converter (ADC) of the spectrometer falls into a Δn range around n_v is assumed to be given by

$$p_{(n_v,\,\Delta n)} = \frac{1}{\sqrt{2\pi}\,\sigma}\int_{n_v-\frac{\Delta n}{2}}^{n_v+\frac{\Delta n}{2}} \exp(-n^2/(2\sigma^2))\,\mathrm{d}n$$

$$\approx \frac{1}{\sqrt{2\pi}\,\sigma}\exp(-n_v^2/(2\sigma^2))\,\Delta n\,. \qquad \text{(A.1)}$$

Here Δn is the step width of the ADC and σ is the root mean square noise voltage at the input of the ADC. Now let us assume that our line finder program built around (1) of the text has reached the center of a Lorentzian hidden in noise. This situation is depicted in Figure A.1. Then the least squares fit of a Lorentzian to the experimental data points leads to the solid line profile shown in this Figure. We now ask for the probability that a sequence of a total of $2\Delta v$ noise-offsets will occur. If the noise-offsets (n_v) at the subsequent data points are truely independent, this probability (P_S) is given by the product of the corresponding $2\Delta v$ individual noise-offset probabilities, each calculated according to (A.1):

$$P_S = \left(\frac{\Delta n}{\sqrt{2\pi}\,\sigma}\right)^{2\Delta v} \exp\left(-\sum_{v=v_0-\Delta v}^{v_0+\Delta v} n_v^2/(2\sigma^2)\right). \qquad \text{(A.2)}$$

We then look at the noisy raw data from two different points of view. First we assume the Lorentzian to be

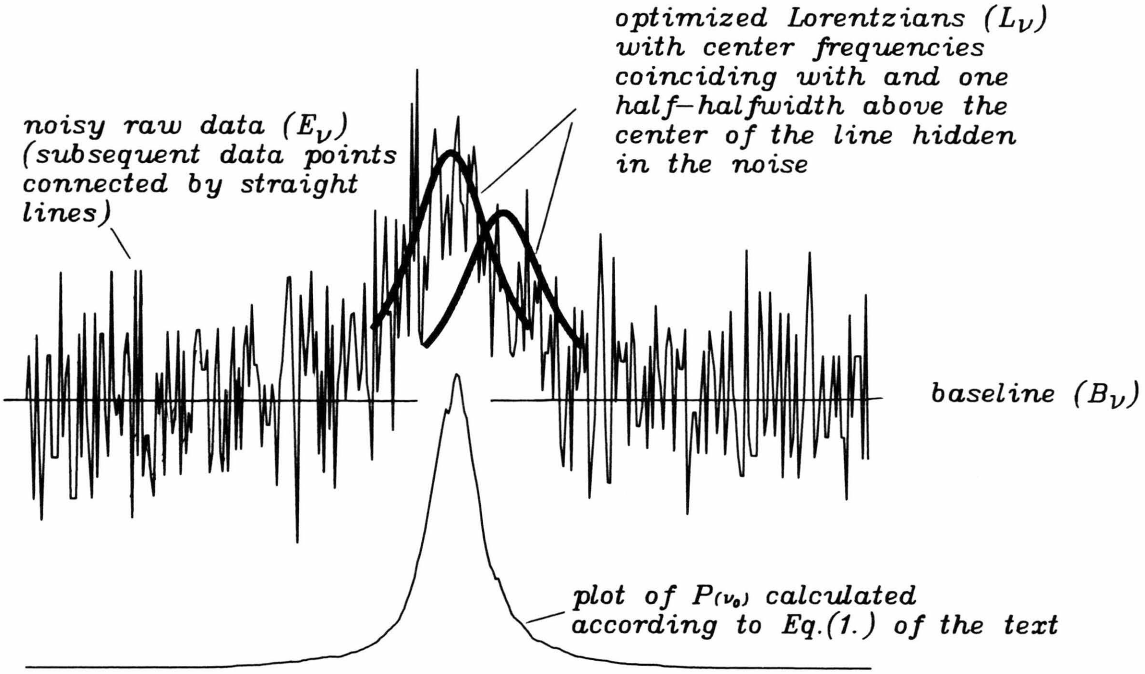

Fig. A 1. Comparison of the experimental data (E_ν) with a hight optimized Lorentzian centered at frequency point ν_0 on the one hand and with the baseline (B_ν) on the other hand gives information on the probability that a line is present at frequency ν_0. In the top trace the center frequency of the Lorentzian (ν_0) coincides with the line center. In the second trace ν_0 is shifted by one half width to higher frequencies. In the bottom trace we have plotted the expression given in (1).

present. In this case the n_ν values are given by the differences between the experimental data points E_ν and the corresponding values of the Lorentzian L_ν:

$$n_\nu = (E_\nu - L_\nu),$$

and we designate the probability for the sequence of the $2\Delta\nu$ noise-offset calculated according to (A.1) with a second index L (for Lorentzian):

$$P_{\mathrm{S,L}} = \left(\frac{\Delta n}{\sqrt{2\pi}\,\sigma}\right)^{2\Delta\nu} \exp\left(-\sum_{\nu=\nu_0-\Delta\nu}^{\nu_0+\Delta\nu} (E_\nu - L_\nu)^2/(2\sigma^2)\right). \tag{A.3}$$

Second we assume that "in reality" there is no line and that the bump in Fig. A.1 is just the result of an admittedly unlikely sequence of large noise offsets. From this point of view we have to set

$$n_\nu = (E_\nu - B_\nu),$$

and we designate the probability for the corresponding offset sequence with B as second index (for baseline):

$$P_{\mathrm{S,B}} = \left(\frac{\Delta n}{\sqrt{2\pi}\,\sigma}\right)^{2\Delta\nu} \exp\left(-\sum_{\nu=\nu_0-\Delta\nu}^{\nu_0+\Delta\nu} (E_\nu - B_\nu)^2/(2\sigma^2)\right) \tag{A.4}$$

(because of the larger offset in the exponents $P_{\mathrm{S,B}}$ is considerably smaller than P_{S} in a situation as depicted in Figure A.1).

Now we are interested in the quotient of the two probabilities. This quotient can also be regarded as the quotient of the probability that there is a line divided by the probability that in reality there is no line. It is given by

$$\begin{aligned} Q_{\mathrm{L/B}} &= P_{\mathrm{S,L}}/P_{\mathrm{S,B}} \\ &= \exp\left(-\sum_{\nu=\nu_0-\Delta\nu}^{\nu_0+\Delta\nu} (E_\nu - L_\nu)^2/(2\sigma^2) \right. \\ &\qquad \left. + \sum_{\nu=\nu_0-\Delta\nu}^{\nu_0+\Delta\nu} (E_\nu - B_\nu)^2/(2\sigma^2)\right). \end{aligned} \tag{A.5}$$

In the presence of a larger line this quotient may become exceedingly large. So we take its logarithm:

$$\begin{aligned} \ln(Q_{\mathrm{L/B}}) &= \ln(P_{\mathrm{L,S}}/P_{\mathrm{S,B}}) \\ &= \sum_{\nu=\nu_0-\Delta\nu}^{\nu_0+\Delta\nu} (E_\nu - B_\nu)^2/(2\sigma^2) - \sum_{\nu=\nu_0-\Delta\nu}^{\nu_0+\Delta\nu} (E_\nu - L_\nu)^2/(2\sigma^2). \end{aligned} \tag{A.6}$$

Now, since the data points of the Lorentzian, L_ν, resulted from a least squares fit to the experimental data points, σ^2 can be roughly calculated from the first sum as

$$\sigma^2 = \frac{1}{2\Delta\nu} \sum_{\nu=\nu_0-\Delta\nu}^{\nu_0+\Delta\nu} (E_\nu - L_\nu)^2 .$$

Inserting this expression into (A.6) leads to

$$\ln(Q_{\mathrm{L/B}}) = \Delta\nu \left(\left(\sum_{\nu=\nu_0-\Delta\nu}^{\nu_0+\Delta\nu} (E_\nu - B_\nu)^2 \right) \Bigg/ \left(\sum_{\nu=\nu_0-\Delta\nu}^{\nu_0+\Delta\nu} (E_\nu - L_\nu)^2 \right) - 1 \right)$$

which is essentially identical with (1) of the text. We note that if ν_0 does not coincide with a line center, a situation also shown in Fig. A.1, the sum $\sum_\nu (E_\nu - L_\nu)^2$ is larger than $2\Delta\nu\sigma^2$. This contributes to the rapid drop of the plotted expression in the wings of a line. In between the lines, the optimized Lorentzian will have zero height and (1) of the text will essentially give zero.

[1] T. G. Schmalz, C. L. Norris, and W. H. Flygare, J. Amer. Chem. Soc. **94,** 7961 (1973).
[2] J. Wiese, Diplom Thesis, Universität Kiel 1975.
[3] M. Schindler and W. Kutzelnigg, J. Chem. Phys. **76,** 1919 (1982).
[4] D. R. Johnson and F. J. Lovas, Chem. Phys. Lett. **15,** 65 (1972).
[5a] R. Pearson, Jr. and F. J. Lovas, J. Chem. Phys. **66,** 4149 (1977).
[5b] William H. Kirchhoff, Donald R. Johnson, and Frank J. Lovas, J. Phys. Chem. Ref. Data **2,** 1–10 (1973); Table 1, p. 3 ($\mu_a = 1.325 \pm 0.020$ D; $\mu_b = 1.53 \pm 0.04$ D).
[6] R. D. Brown, P. D. Godfrey, and D. A. Winkler, Aust. J. Chem. **35,** 667 (1982).
[7] W. H. Stolze, Dissertation, Universität Kiel 1988.
[8] Such a procedure was suggested by R. D. Brown at the 1985 Colloquium on High Resolution Molecular Spectroscopy held at Riccione, Italy.
[9] D. H. Sutter, Z. Naturforsch. **26a,** 1644 (1971).
[10] D. H. Sutter and W. H. Flygare, The Molecular Zeeman Effect, Topics in current Chem. **63,** Chapt. III.A (1976).
[11] W. Gordy and R. L. Cook, Microwave Molecular Spectra, 3rd Edition, John Wiley, New York 1984.
[12] W. H. Flygare, J. Chem. Phys. **41,** 793 (1964).
[13] W. H. Flygare, Molecular Structure and Dynamics, Prentice-Hall, Inc., Englewood Cliffs, New Jersey 1978, Chapter 6.9.
[14] M. Stolze, D. Hübner, and D. H. Sutter, Z. Naturforsch. **36a,** 886 (1981).
[15a] Kazuo Kitaura, Yoshihiro Osamura, and Kichisuke Nishimoto, Chem. Phys. Lett. **63,** 406 (1979).
[15b] R. Macaulay and L. A. Burnelle, Theoret. Chim. Acta **29,** 1 (1973).
[15c] Robert Ditchfield, Janet E. Del Bene, and J. A. Pople, J. Amer. Chem. Soc. **94,** 703 (1972).
[16] R. Barnes and W. H. Smith, Phys. Rev. **93,** 95 (1954).
[17] M. Stolze and D. H. Stutter, Z. Naturforsch. **40a,** 998 (1985).
[18] D. H. Sutter and W. H. Flygare, J. Amer. Chem. Soc. **91,** 6895 (1969).
[19] J. R. Eshbach and M. W. P. Strandberg, Phys. Rev. **85,** 24 (1952).
[20] J. H. Van Vleck, The Theory of Electric and Magnetic Susceptibilities, Oxford University Press, Oxford, England 1932.
[21] W. Hüttner, M. K. Lo, and W. H. Flygare, J. Chem. Phys. **48,** 1206 (1968).
[22] L. Engelbrecht and D. H. Sutter, Z. Naturforsch. **33a,** 1525 (1978).
[23] R. E. Moss and A. J. Perry, Mol. Phys. **25,** 1121 (1973).
[24] E. Hamer, L. Engelbrecht, and D. H. Sutter, Z. Naturforsch. **29a,** 924 (1974).
[25] R. P. Blickensderfer, J. H. S. Wang, and W. H. Flygare, J. Chem. Phys. **51,** 3196 (1969).
[26] Z. B. Maksic and N. Mikac, J. Mol. Struct. **44,** 255 (1978).
[27] M. F. Guest, J. Kendrick, and S. S. Pope, in: GAMES Users Manual, SERC Daresburg Laboratory, DL/SCI TMOOOT (1986). – M. Dupuis, D. Spangler, and J. Wendoloski, NRCC Software Catalog, Vol. 1, Program No. QC01 (GAMESS) (1980).
[28] M. Redshaw, M. H. Palmer, and R. H. Findlay, Z. Naturforsch. **34a,** 220 (1979).
[29] M. H. Palmer, I. Simpson, and R. H. Findlay, Z. Naturforsch. **36a,** 34 (1981).
[30] J. T. Hougen, J. Chem. Phys. **57,** 4207 (1972), Table VII.
[31] M. Rodler, R. D. Brown, P. D. Godfrey, and B. Kleibömer, J. Mol. Spectr. **118,** 267 (1986).
[32] E. Kochanski, J. M. Lehn, and B. Levy, Theor. Chim. Acta **22,** 111 (1971).
[33] M. H. Palmer, R. H. Findlay, and A. J. Gaskell, J. Chem. Soc., Perkin Trans. **II,** 420 (1974).